Simulation of an ethylene wall fire using the spatially-evolving one-dimensional turbulence model

Abstract The mechanism of flame propagation in fuel beds of wildland fires is important to understand in order to quantify fire spread rates. Fires spread by radiative and convective heating and often require direct flame contact to achieve ignition. The flame interface in an advancing fire is unsteady and turbulent, making study of intermittent flames in complex fuels difficult. A vertical wall fire, in which ethylene fuel is slowly fed through a porous ceramic, is modeled to investigate unsteady turbulent flames in a controlled environment. Simulations of this configuration are performed using a spatial formulation of the one-dimensional turbulence (ODT) model which is able to resolve individual flames (a key property of this model) and provide realistic turbulent statistics. ODT solves diffusion-reaction equations along a notional line of sight perpendicular to the wall that is advanced vertically. Turbulent advection is modeled through stochastic domain mapping processes. Simulations include radiation and soot effects and are compared to experimental temperature data taken over a range of fuel flow rates. Flame structure, velocities, soot, and temperature statistics are reported. The ODT model is shown to capture the evolution of the flame and describe the intermittent properties at the flame edge.

Keywords Wall flame · Ethylene · one-dimensional turbulence · fire

1 Introduction

This paper presents comparisons of simulations using the one-dimensional turbulence model to experimental data of an ethylene wall fire. Wall fires are important in their own right, but the principal motivation of this study arose from flame propagation in wildland fires.

Understanding the mechanism of flame propagation in wildland fires is important for developing accurate fire models to predict fire behavior. In general, radiation has been noted as the principal heat transfer mechanism for flame front

Address(es) of author(s) should be given

propagation through an unburnt fuel bed [1]. However, several studies have suggested that radiative heat transfer is not sufficient in heating fuels to ignition, but that additional heat transfer methods are required [2–4]. Recent experiments and observations indicate the importance of convective heating by direct flame contact [5]. For instance, Cohen and Finney [6] demonstrated preferential ignition of large diameter fuels over fine fuels exposed to the same radiative source since convection of surrounding air (induced by buoyant acceleration at the heat source) allows cooling of the fine fuel.

Flame propagation by convective heating of unburnt fuel through direct flame contact is a complex process influenced by many factors. The scales in fires are large enough that the flows are nearly always turbulent, with the flow driven by buoyant acceleration in the flame zone and wind effects [2]. Turbulent flames involve (by definition) a wide range of time and length scales, ranging from sub-millimeter flames to scales as large as the fire itself–tens of meters in forest crown fires. Individual flames that occur at turbulent dissipation scales involve many differentially-diffusing species whose identity and chemical reaction mechanisms may be unknown. Soot formation and radiative transport further complicate the process. The propagation of the flame front is unsteady, with intermittent turbulent flames in fuel beds consisting of complex fuel and spatial distribution. Hot combustion gases have lower density than surrounding air, resulting in gas expansion. This expansion causes an incline in the flame front. Excursions of flame into unburnt fuel, enhanced by an inclined flame front, have been shown to result directly in fuel ignition and subsequent flame propagation [7].

This paper is part of a larger study of the fundamentals of fire propagation in fuel beds. To capture flame propagation by direct flame contact, the turbulent flame itself must be resolved. The only simulation approach that can resolve flames in turbulent flows is direct numerical simulation (DNS), which is prohibitively expensive (computationally) at fire scales. RANS and LES approaches can capture the fire scales, but cannot resolve individual flames. The one-dimensional turbulence model (ODT) is applied in this study because it is able to resolve all of the length and time scales (from the fire scale to individual flamelets), but in a single dimension so that the model is computationally efficient. The ODT model solves reaction-diffusion equations for mass, momentum, species, and energy, on a notional line-of-sight through a flow. Turbulent advection is modeled in ODT using a stochastic domain remapping process that simulates the effect of eddies. The model is described further below, but the key point is that it is able to resolve individual flames with realistic turbulence statistics.

The ODT model has been widely applied to many reacting and non-reacting flows including homogeneous turbulence [8], mixing layers [9], channel flow [10], Reyleigh-Benard convection [11], and double diffusive interfaces [12] to name a few. Dreeben and Kerstein [13] modeled buoyant heat transfer in a vertical slot. Several researchers have studied turbulent jet flames with ODT including effects of flame extinction and reignition using several fuels [14–18]. Of direct relevance to the present study, Ricks et al. [19] modeled soot and enthalpy evolution in buoyant pool fires. Shihn and DesJardin [20] used ODT to simulate a buoyant, isothermally heated wall. These authors also studied near-wall behavior of vertical wall fires with acetylene and propane fuels to demonstrate ODT as a possible sub-grid closure model for LES [21]. Other studies using ODT as an LES sub-grid model include [22–25]. Because ODT is one-dimensional, it is best suited to temporally-evolving

one-dimensional flows, or to two-dimensional statistically steady flows. That is, flows that can be approximated by boundary layer assumptions. The ethylene wall flame varies primarily in the wall-normal direction with vertical velocities dominant.

The complexity of fires necessitates simplified fuels and configurations amenable to experimental investigation and model validation. In this paper a wall fire is studied because it adds fuel to the system with height, which approximates the behavior of a buoyantly-driven flame front inclined by gas expansion. This stationary configuration eases setup and data collection. While many studies have been done on wall fires, most of them focus on the burning rates along the wall rather than the turbulent, intermittent statistics away from the wall. Ahmad and Faeth [26] studied burning rates in wall fires, where the burning surface was simulated by a fuel soaked wick. Markstein and De Ris [27] measured radiative emission from porous metal wall burners using several fuels. Quintiere [28] developed a framework for modelling flame spread rates along a vertical wall using a zone method. Delichatsios [29] studied pyrolysis/burning rates and flame heights of wall fires using a two-layer integral model. Joulain [30] studied flame propagation, burning rates, and mean temperatures and velocities present in vertical wall fires. One study by Wang et al. [31] focused on the turbulent, intermittent statistics away from the wall. This study used LES to investigate the transport characteristics and flame structures of vertical wall fires. As LES is a filtered model, the small scales were not resolved and a sub-grid model was used in this approach.

Recent experiments were performed by Finney et al. [5] of a vertical wall flame with ethylene fed uniformly through a porous ceramic burner to study properties at the intermittent flame interface. Instantaneous temperature measurements were made at four vertical stations and six horizontal positions for several fuel flow rates.

This work simulates the experimental configuration using the ODT model. We present results of the model including velocity and temperature profiles. Mean and fluctuating distributions are also given, along with sensitivity to model variations.

This work represents an extension of the ODT model in terms of the complexity of the configuration considered and is the first application of the formal spatial implementation of ODT [32] to reacting wall-bounded flows. (Application to a nonreacting isothermal wall was performed in [33].) Beyond this study, the successful application of ODT to buoyantly-driven, wall-bounded flows is important and would allow, e.g., detailed wall heat transfer studies.

2 Experimental configuration

The ethylene wall fire experiments are described in [5]. A summary is provided here. The experimental wall burner consists of an inner sintered metal layer, followed by a porous ceramic foam [5]. The burner dimensions are 1.83 m tall, and 0.61 m wide. A fiberglass cloth borders the burner assembly in the plane of the burner. Ethylene flow rates range from 115-470 standard L/min. These flow rates correspond to heat release rates of 106-435 kW. Flow rates of 235, 390 and 470 L/min are studied here. Ethylene was chosen because its molecular weight is close to that of air, so that uneven flow distribution due to hydrostatic pressure was avoided. Ethylene combustion also conserves moles so that density differences are due to temperature effects. Figure 1 shows a schematic of the configuration. In the
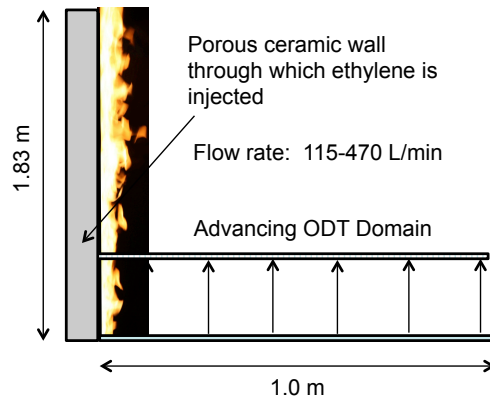
Fig. 1 Schematic of the ethylene wall fire configuration.

simulations, the ODT domain is oriented horizontally and is perpendicular to the wall. The solution is evolved by marching the ODT domain upwards, described further below.

Temperature measurements were made at four heights up the wall. At each height, a set of six 0.00508 cm diameter type-K thermocouples were spaced horizontally at varying distances from the vertical wall. The temperature measurements were made at heights of 0.35, 0.78, 1.23, and 1.69 m. At the first height, the six thermocouples were placed at distances of 3, 5, 7, 9, 11, and 13 cm from the wall. At the other three heights the six thermocouples at each height were placed at 4, 6, 8, 10, 12, and 14 cm from the wall. The measured response time of the thermocouples in 5 m/s moving air was approximately 50 ms. The thermocouples were connected to a National Instruments Inc. SCXI 1102B module in the data acquisition system with a sensor bandwidth of approximately 3 Hz.

3 Model formulation

A brief overview of ODT is presented here. A detailed description of the ODT formulation and implementation used here is available in the literature [33,9,32].

3.1 ODT model

ODT solves two concurrent processes: (1) advancement of one-dimensional reaction-diffusion equations for mass, momentum, energy, and chemical species; and (2) turbulent advection modeled through stochastic eddy events consisting of a domain remapping process. There are two formulations of ODT: temporal and spatial. In temporal ODT, the one-dimensional domain is evolved in time. In spatial ODT, the domain is advanced in a spatial coordinate perpendicular to the line, and a steady state solution is assumed. In both cases the system is parabolic. Here, the spatial formulation of ODT is used, but the presentation below is given for the temporal formulation, then adapted to the spatial formulation.

Turbulent advection is modeled stochastically with domain remapping processes, called eddy events, that are implemented through triplet maps. A turbulent eddy is modeled as having a size l, location x_0, and timescale τ. A given eddy event is implemented using a triplet map by replacing original property profiles in the eddy region with three copies of the profiles, each spatially compressed by a factor of three, with the center copy spatially mirrored. This retains key turbulent processes of increasing gradients and surface area, while all properties are conserved and profiles are continuous. Eddy events are selected using a thinning process [34] based on the rejection method [35]. Candidate eddies are drawn from a presumed eddy size l and location x_0 distribution $P(x_0, l)$ and accepted with probability

$$P_a = \frac{\Delta t_s}{\tau P(x_0, l) l^2}.$$ (1)

The specification of $P(x_0, l)$ affects the efficiency of the model, but not the accuracy. Candidate eddies are sampled in time as a Poisson processes with rate $1/\Delta t_s$. In Equation (1), τ is the eddy timescale, computed as

$$\frac{1}{\tau} = C \left[\frac{2}{\rho_0 l^3} (E_{kin} - Z E_{vp} + E_{DL}) \right]^{1/2},$$ (2)

which is based on the one-dimensional scaling $E \sim \frac{1}{2} \rho_0 l^3 / \tau^2$, where $\rho_0 = \frac{1}{l^3} \int \rho K(x)^2 dx$ and $K(x)$ is a kernel function that is the difference in final and initial locations defined by the triplet map [9,32]. The E_{kin} term is a measure of the kinetic energy within the eddy interval and is specified as in [32]. The E_{VP} term is a viscous penalty introduced to suppress small eddies subject to strong viscous damping, modeled as $E_{vp} = \frac{1}{2} \bar{\mu}^2 / \bar{\rho} l$, where $\bar{\mu}$ and $\bar{\rho}$ are the average viscosity and density in the eddy region, respectively. C and Z in Equation (2) are the adjustable eddy rate and viscous penalty parameters, respectively. E_{DL} is a new term that models the Darrieus-Landau combustion instability, described below.

In the spatial formulation used in this paper, the sample time Δt_s is replaced by a spatial increment Δy_s, and τ is converted to an eddy length scale by multiplying by the Favre-mean velocity $\tilde{U}$ in the eddy region. In addition, kernel operations, as in the calculation of ρ_0 above, and E_{kin} include the local velocity in the integral ($\rho u(x)$ instead of ρ) since mass flux, not mass is the key quantity in the spatial formulation [32], discussed further below. A large eddy suppression mechanism is used to prevent unphysically large eddies from occurring. Several models are possible; here, we use the criteria $y > \beta l$, where β an adjustable parameter.

Spatial ODT advances the horizontal line up the wall instead of advancing in time. The flow is assumed steady, except for the stochastic eddy events, that is, the flow is evolved in the downstream direction parabolically using standard boundary layer assumptions. The ODT code used is described in [33]. The code is written in C++ and uses an adaptive mesh. The diffusive advancement uses a Lagrangian finite volume formulation in which cells expand or contract such that the total vertical mass flux in a given cell is constant: $\rho v \Delta x = c$, which is the result of the continuity equation applied to the cells. Other transport equations for species mass fractions, vertical momentum, and enthalpy in a given grid cell,

are given, respectively, by

$$\frac{dY_k}{dy} = -\frac{j_{k,\,e} - f_{k,\,w}}{\rho v \Delta x} + \frac{\omega_k}{\rho v}, \tag{3}$$

$$\frac{dv}{dy} = -\frac{\tau_e - \tau_w}{\rho v \Delta x} + \frac{(\rho_\infty - \rho)g}{\rho v}, \tag{4}$$

$$\frac{dh}{dy} = -\frac{q_e - q_w}{\rho v \Delta x} + \frac{S_{rad}}{\rho v}. \tag{5}$$

Here, y is the vertical direction and x is horizontal. Subscripts e and w denote cell face values. The momentum flux is modeled as $\tau = -\mu(dv/dx)$, and the species mass flux is modeled as $j_k = -(\rho Y_k D_k / X_k)dX_k/dx$, where X_k is a species mole fraction and D_k is the binary diffusion coefficient. Heat flux is given by $q = -\lambda dT/dy + \sum_k h_k j_k$, where λ is the thermal conductivity, and h_k is the enthalpy of species k. The division by $\rho v \Delta x$ in the above equations follows from $\rho v \Delta x = c$. This relation is used to specify how changes in v and ρ affect the grid size Δx. In the spatial advancement of the ODT line, grid cells with smaller velocities have an implied larger residence time ($\Delta t = \Delta y / v$). Ideal gases are assumed, and temperature is related to enthalpy through the auxiliary relation $h = h(T, Y_i)$ using composition and temperature dependent heat capacities. Cantera is used for all thermochemical and transport properties [36]. The source term ω_k is the species reaction rate, and S_{rad} is the radiative source term.

The ODT code is solved using a first order explicit spatial advancement, with central difference approximations used for spatial derivatives appearing in flux terms. The advancement step Δy is small enough that no changes are apparent when using a second order trapezoidal spatial advancement. Mean chemical source terms (used in the explicit advancement) are computed with a high order implicit method using CVODE [37] with constant cell fluxes. This eliminates chemical stiffness and allows advancement at the diffusive CFL. The adaptive mesh approach is applied by merging and splitting grid cells in a manner that conserves vertical fluxes of transported quantities: mass, momentum, thermal energy, and soot. The grid is adapted based on a nominally uniform distribution of grid points along the arc length of the (centered and scaled) temperature, velocity, and soot profiles (velocity temperature, or soot is chosen based on the highest local grid refinement) [33]. A minimum grid cell size of 100 μm is used, which is sufficiently small that no significant differences in results are observed when doubling the number of grid cells.

3.2 Darrieus-Landau instability

Buoyant forces may arise in a fluid for which there are density gradients and a body force. In the case of the Rayleigh-Taylor instability, density gradients are due to temperature gradients, such that heavy fluid is above light fluid, and the body force acting is gravity. Similarly, in a reactive flow, planar flames are intrinsically unstable due to acceleration of the variable-density fluid caused by thermal expansion across the burning front. This instability is termed the Darrieus-Landau (DL) instability. Using the analogy to Rayleigh-Taylor instability allows an existing ODT representation of the Rayleigh-Taylor instability [38] to be modified in order to

incorporate the Darrieus-Landau instability mechanism into ODT. Namely, a formal analog of gravitational potential energy is introduced. In the present case, the constant acceleration of the gravity is replaced by the varying dilatation-induced acceleration on the line. The DL potential energy is then defined as

$$E_{DL} = \frac{8}{27} \int_{x_0}^{x_0+l} a(x)K(x)(\rho(x) - \bar{\rho})dx, \tag{6}$$

where the factor 8/27 arises due to the variable density formulation and $\bar{\rho}$ is a reference density defined as the average density over the interval $[x_0, x_0 + l]$. This potential energy is nonzero only where the density varies, as it is the interaction of the dilatation-induced pressure gradient and the density gradient that is the cause of this instability mechanism. E_{DL} is not a potential energy in the same sense as in a buoyant flow, because it is not based on an external energy source. For this reason, it is only used to effect the probability of acceptance of an eddy. It is however, a formal analog to the treatment of energy in the buoyant flow, and therefore a tunable coefficient is not required.

It is interesting to note ODT allows explicit specification of physical effects such as the DL instability based on flow energetics, so that such effects may be studied directly. This is not as easily studied in Navier-Stokes-based solution approaches.

3.3 Chemical mechanism

The ODT model can solve arbitrarily complex combustion mechanisms. The results presented are based on a global one-step mechanism that captures overall flame heat release [39]. Combustion timescales are fast compared to mixing timescales in the flames studied and finite rate kinetic effects are minor. The chemical mechanism reacts ethylene with oxygen to produce water and carbon dioxide and C_2H_4, O_2, N_2, CO_2, and H_2O are transported. Results are also presented comparing the one-step mechanism to a reduced mechanism consisting of 19 transported species, 10 quasi-steady species, and 167 reactions [40].

3.4 Soot model

The soot model applied is that of Leung et al. [41], which is a semi-empirical four-step model that has been applied in many studies of turbulent, nonpremixed flames. The model assumes a monodispersed size distribution and transports the first two moments of the size distribution: number density n and mass fraction Y_s. Here, moments per mass are transported:

$$\frac{dM_k/\rho}{dy} = -\frac{j_{k,e} - f_{k,w}}{\rho v \Delta x} + \frac{S_k}{\rho v}, \tag{7}$$

where M_k is one of $M_0 = n$ or $M_1 = \rho Y_s$ The soot fluxes consist of thermophoretic transport and are given by $j_k = -(0.554M_k\mu/\rho T)dT/dx$. Soot source terms are taken from [41]. The nucleation and growth species in the Leung model is acetylene. Because there is no acetylene in the one-step mechanism, acetylene was computed using a lookup table parameterized by mixture fraction and heat loss (defined as

the local enthalpy defect from adiabatic normalized by the local adiabatic sensible enthalpy) with streams at 1 atm and 298.15 K. The table was generated with a steady laminar flamelet model [42] using the reduced mechanism noted above.

3.5 Radiation model

The radiative source term in the enthalpy equation is computed using the Schuster-Schwarzchild approximation [43] (two-flux model) which is well suited to ODT in a boundary-layer-like flow. The outgoing (from the wall) heat flux q^+ and incoming heat flux q^- are given by

$$\frac{dq^+}{dx} = 2k\sigma T^4 - 2kq^+,$$
(8)

$$\frac{dq^-}{dx} = -2k\sigma T^4 + 2kq^-.$$
(9)

The surrounding emissivity is unknown, but is set to 1.0. The wall emissivity is set to unity since the wall is covered with a black soot. The absorption coefficient is the sum of gas and soot components: $k = k_g + k_s$. Temperature-dependent Planck mean absorption coefficients are taken for gas species CO_2, CO, CH_4, and H_2O [44], with $k_g = \sum_i k_i P_i$. The soot absorption coefficient is taken as $k_s = 1863 f_v T$.

3.6 Boundary and initial conditions

The initial velocity field is simply a uniform profile of magnitude 0.05 m/s, which is less than 1% of the peak mean velocity evolved. The flame is initialized by specifying an initial mixture fraction profile $\xi(x)$, which is set using a hyperbolic tangent varying from nominally one at the wall to zero in the air. $\xi = 1$ is pure ethylene, and $\xi = 0$ is air. The transition width is 5 mm and its center is 5 mm from the wall. The initial composition profiles are taken as products of complete combustion, with temperature following from the known $h(\xi)$ relation and the composition. Results were not found to be sensitive to the initial velocity and mixture fraction profiles. The ambient temperature and pressure are set to 298.15 K and 90143 Pa, respectively. Ethylene enters through the wall at 298.15 K. Ethylene flow rates of 235, 390, and 470 standard L/min are studied, which correspond to wall flow velocities of 3.944, 6.545, and 7.888 mm/s, respectively. The wall is assumed adiabatic and diffusive species mass fluxes are assumed zero at the wall. The divergence of the soot flux is set to zero at the wall. All diffusive fluxes are assumed zero at the outlet boundary in the free stream.

4 Results

A number of simulations were performed to test the model and compare to available experiments. The simulation cases are summarized in Table 1. Baseline parameters are specified and individual cases are represent variations from the baseline.

Table 1 Summary of simulation cases and parameters.

Baseline Parameters		Case	Baseline Variation
Fuel Flow (L/min)	390	1	235 L/min, 256 Rlz
Chemistry	1-step	2	512 Rlz
BC	adiabatic	3	490 L/min, 256 Rlz
C	10	4	C=5
Z	400	5	C=20
β	12	6	Z=200
# Realizations (Rlz)	128	7	Z=800
		8	$\beta = 6$
		9	$\beta = 24$
		10	BC=isothermal
		11	No DL mechanism
		12	Reduced chemistry

Simulations were performed at the Fulton Supercomputing Laboratory at Brigham Young University on 2.8 GHz Intel Nehalem processors. The average simulation time per realization for Case 2 was 0.93 hours. Other cases are similar except Case 12, which is the reduced mechanism case and had a mean simulation time of 8.0 hours.

Figure 2 shows contours of temperature for a single typical realization. The effect of triplet maps is shown, which cause intermittency in the flame. Buoyancy causes an upward acceleration of the flow, which draws in surrounding air. This is observed by the contraction of the flame, which is imposed by the conservation of upward mass flux. Buoyant acceleration tends to cause horizontal contraction of the flow, and is opposed by flame dilatation from heat release which expands the flow. The occurrence of eddy events spreads the flame outward from the wall. While the mean profiles will be concentrated relatively close to the wall, it is clear that intermittent flame zones are present farther from the wall. Figure 2 also shows the size and location of eddies for this particular realization. A wide range of eddies occur as indicated in the figure. The eddies are concentrated in regions of higher shear and lower velocities, which imply higher residence time. This occurs in regions of the flame that are lean of the peak temperature, away from the wall. In the vicinity of the peak temperature the velocity passes through a maximum (see Fig. 5 below), which both reduces shear and residence time for the fluid in this region. It is noted that while the visible portion of the flame (where soot concentration and temperature are high) is clearly turbulent, much of the turbulent mixing occurs outside the flame zone where luminous soot is not present.

Wall-normal scalar profiles for a given realization at a height of 1.8 m (at the top of the wall) are show in Fig. 3. The symbols in the plots indicate the grid spacing. The adaptive grid places many more points in regions of high fluctuations. The temperature and velocity profiles are qualitatively similar with velocities higher in regions of higher temperature due to buoyant acceleration. The magnitude and wavelength of fluctuations is also similar for the velocity and temperature due to the similarity in the thermal and momentum diffusivities. In contrast, the soot mass fraction is highly intermittent with very fine fluctuations owing to the relatively low diffusivity of the soot particles. Resolving such fluctuations is a challenge in turbulent combustion modeling, as is accounting for the interactions between
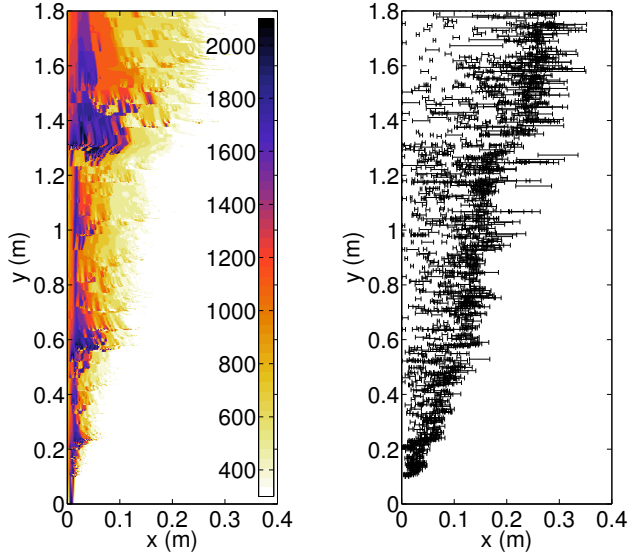
Fig. 2 Temperature and eddy size and location renderings for a single ODT realization for Case 2. Leftward and rightward sweeps of temperature iso-contours reflect buoyancy-induced contraction and dilatation-induced expansion, respectively.

the soot, temperature, and radiative fields. The ability of ODT to capture fine scale fluctuations provides great opportunity to study and model such interactions.

Mean and root mean square (RMS) fluctuations of temperature, velocity, and soot are shown in Fig. 4 as contour plots for Case 2. The maximum mean temperature is approximately 1600 K, not including the initial condition. While the peak temperature remains relatively close to the wall, the temperature profile is observed to spread significantly. This is mirrored by the RMS profile, with higher values penetrating farther into the free stream. The peak RMS temperature ($\approx$400 K) occurs near the base of the wall as the turbulent eddies first wrinkle the initial flame.

The mean soot field shows broad spreading, but is highly concentrated to the rich side of the flame near the wall where the soot is formed. This is on the wall side of the peak mean temperature within 2 cm of the wall. The peak mean soot mass fraction is 0.009, which corresponds to a soot volume fraction (assuming ρ_s=1850 kg/m^3) of 1.8 ppmv. The RMS soot mass fraction is close to the mean, with the peak RMS soot mass fraction at 0.0037, and a peak RMS soot volume fraction of 0.4 ppmv. These values for the mean and RMS are taken at $y = 1.8$ m, near the top of the wall.

The mean horizontal velocity profile for Case 2 in Fig. 4, shows a steady increase, both in magnitude and in width. The velocity increases due to buoyant acceleration. As the mean velocity increases, the RMS fluctuations also increase, with fluctuations around 10% of the mean values. The fluctuations in the tempera-
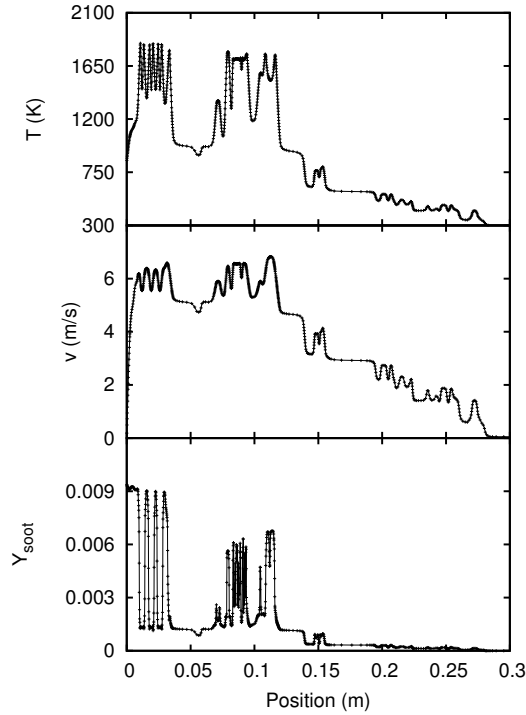
Fig. 3 Profiles temperature, velocity, and soot mass fraction for a single realization for Case 2 at $y = 1.8$ m.

ture, soot, and velocity fields all peak at higher x locations than the corresponding mean values.

Figure 5 shows horizontal profiles of the vertical velocity at four heights in the flame for Case 2. The mean velocity profile rises from zero at the wall and reaches a peak of 6 m/s near the top of the wall at 1.69 m, then decreases, nearly linearly towards the free stream. The figure also shows the velocity profiles scaled by the peak mean values at each height with the line position scaled by the profile width taken as the full width at half the maximum (fwhm). The scaled profiles are self-similar and collapse to a single curve, though somewhat less for profile at y=35 cm where the velocity is developing. This similarity is consistent with previous wall fire reports [26,29] and an isothermal wall previously studied with ODT and compared to experiments [20,33].

The mean and RMS temperature profiles are compared to the available experimental data for Cases 1-3, with flow rates of 234, 390, and 470 L/min. The results for the means are presented in Fig. 6. The figure shows profiles at the four measurement heights of 35, 78, 123, and 169 cm. The peak temperatures are similar

(a) mean T, K (b) mean v, m/s (c) mean Y_s

(d) RMS T, K (e) RMS v, m/s (f) RMS Y_s
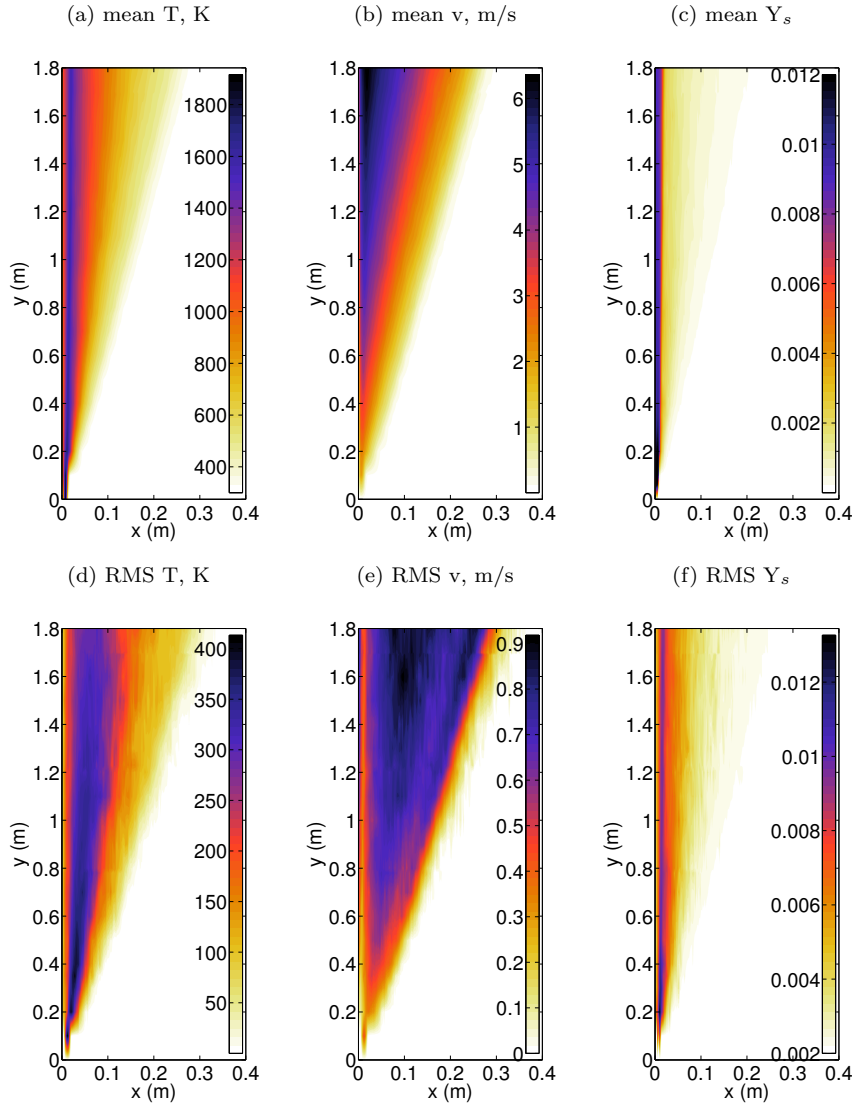
Fig. 4 Temperature (a), (d), vertical velocity (b), (e), and soot mass fraction (c), (f) profiles. Top row: means, (a), (b), and (c); bottom row: RMS (d), (e), (f), for Case 2.

for the three flow rates and at the three heights, though there is a small decrease in the peak temperature with increasing flow rate (due to enhanced mixing), and with height due to mixing and radiative losses. The location of the peak temperature increases from the wall with increasing flow rate. Similarly, the temperature on the air side of the peak, in the measurement region, increases with increasing flow rate as the width of the flame brush increases. The ODT comparison to the experiments is seen to be good. At a given height and horizontal distance, the

(a)   (b)
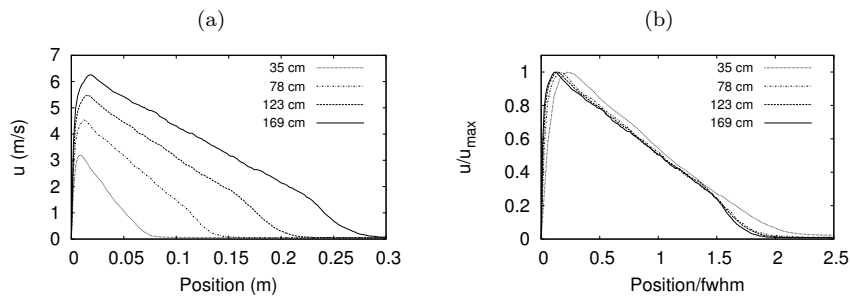
Fig. 5 Case 2 mean vertical velocity profiles for Case 2 at four heights (a), and the same velocity profiles scaled by the max mean values and the profile widths (evaluated as the full width at half maximum, fwhm) at each height (b).
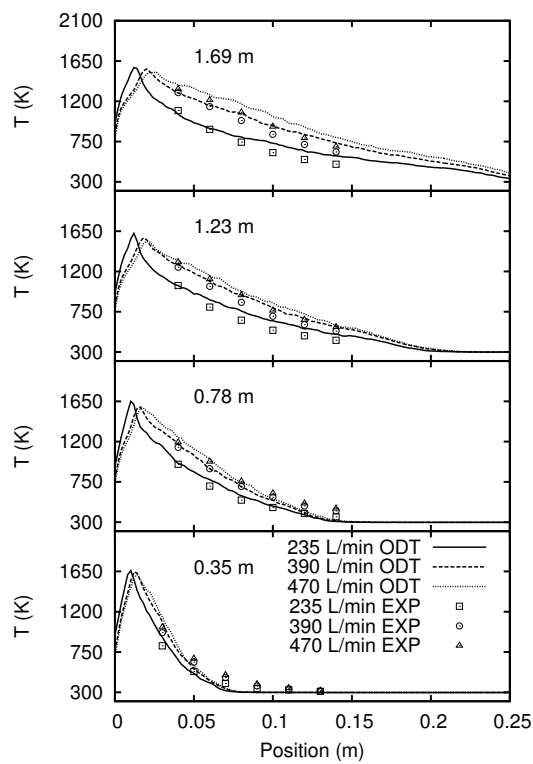
Fig. 6 Mean temperature profiles for three flow rates comparing the ODT simulations (lines) to the experiments (symbols). Four plots shown at increasing height.
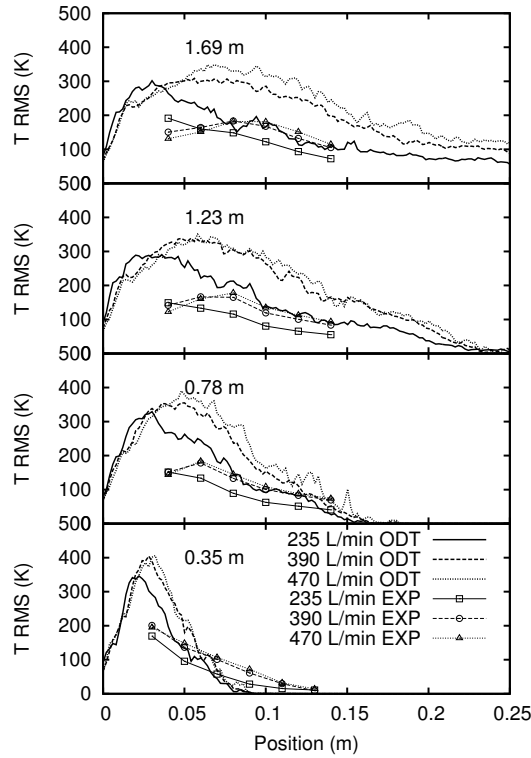
Fig. 7 RMS temperature profiles for three flow rates comparing the ODT simulations (lines) to the experiments (symbols). Four plots shown at increasing height.

spread in the data with flow rate is closely matched by the spread in ODT results. At 35 mm, where the flow is presumably developing, the ODT does not spread horizontally as fast as the experimental temperatures. At the highest position, the ODT spreads somewhat more than the experiments.

These results are somewhat dependent on the ODT parameters, and slightly better experimental agreement is obtained using C=5, as shown in Fig. 8 below. Furthermore, while the agreement presented is fairly good, we emphasize the complexity of the physical phenomena and modeling uncertainties. These include the soot formation, radiative transport, chemistry modeling, boundary conditions, and modeling the turbulent advection. An ongoing research effort is to investigate these processes, including model sensitivities and interactions. The resolution available in ODT can help address such issues, especially when coupled with experiments, DNS, and LES.

Figure 7 shows the RMS temperature fluctuations and is similar to Fig 6. The horizontal location of the peak in the RMS increases with height and flow rate. Generally, the peak RMS temperature is higher for the higher flow rates. The trend

in the ODT results matches the experiments, including the crossover of the low flow rate as the wall is approached. The horizontal location of the peak is lower for the ODT than for the experiments, but they are similar at $y = 1.69$ m. As for the mean profiles, the spread is smaller at $y = 0.35$ m. At the upper locations, the shape of the profiles is very similar. The magnitude of the ODT simulation results is higher than the experiments. It is noted that experimental results were obtained using type-K thermocouples whose upper range of around 1600 K is not high enough to accurately capture peak flame temperatures. The time-dependent experimental data did not have any temperatures higher than 1663 K, while the model predicted intermittent temperatures as high as 2000 K. If higher experimental peak temperatures were measured, then the experimental RMS fluctuations would be higher. The thermocouple response time and bandwidth may also affect the comparison with lower response times and higher bandwidth tending to increase RMS fluctuations. This is discussed further in Section 4.4.

4.1 Parameter sensitivity

A sensitivity study was performed in which the three ODT parameters C, Z, and β were varied. These are Cases 2, 4-9 in Table 1. With Case 2 as a baseline, each parameter was increased and decreased by a factor of two. Figure 8 shows results comparing the mean temperature at $y = 1.69$ m. Increasing the eddy rate parameter C results in more eddies and a higher mixing rate, resulting in higher temperatures and a wider flame brush with increasing C. Using C=5 gives slightly better results than C=10. There is very little sensitivity of the results to variation of the Z parameter. Variation of the β parameter shows a higher sensitivity than the other two parameters, with increasing β restricting eddy size and resulting in lower temperatures near the wall, higher temperatures for x between the peak and approximately 0.1 m, and lower temperatures for x greater than 0.1 m. These results suggest that the fire evolution is largely controlled by the large eddies.

4.2 Chemistry and boundary condition sensitivity

The effect of the gas chemistry model is evaluated by comparing the mean temperature and soot profiles using the 1-step and reduced mechanisms. Fig. 9 shows the mean temperature profiles at $y = 1.69$ m. The results are nearly identical for the two mechanisms, with small variation occurring near the wall on the rich side of the flame. The soot concentrations are nearly identical for the two mechanisms in this region of the flame.

The effect of using an isothermal (298 K) wall boundary condition was also tested and is shown in Fig. 9. The mean temperature with the isothermal boundary condition is lower than the adiabatic profile by an average of 83 K for $0 < x < 0.25$ m. The lower isothermal temperature results in a soot concentration about half of that of the adiabatic case.
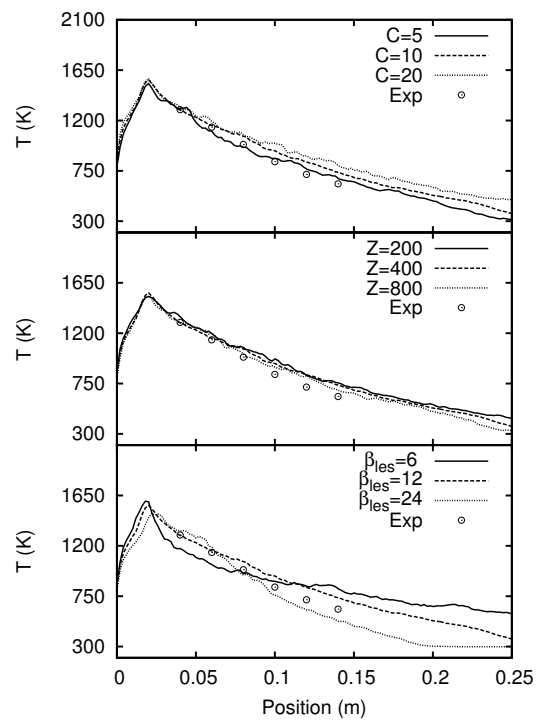
Fig. 8 Sensitivity to ODT parameters at $y = 1.69$ m.
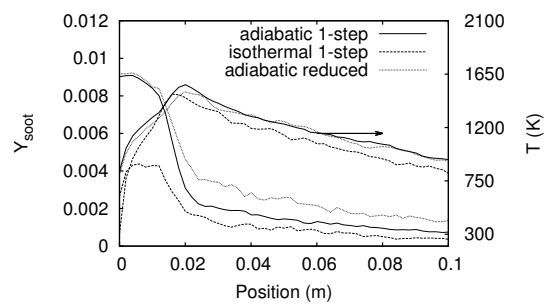
Fig. 9 Mean temperatures at $y = 1.69$ m for two chemical mechanisms, and for two boundary conditions.
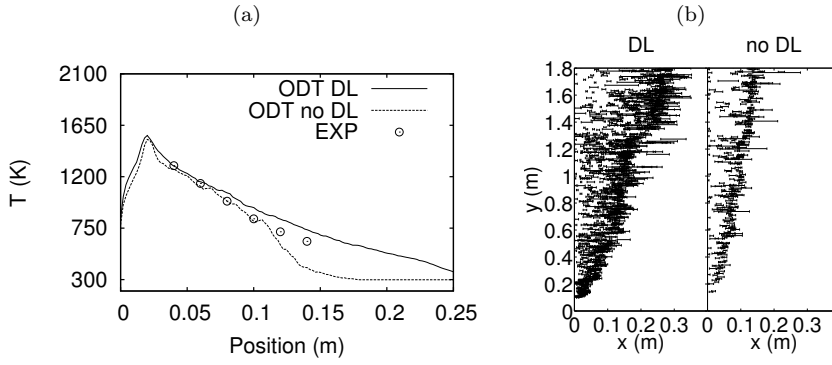
Fig. 10 Mean temperatures at $y = 1.69$ m with and without the Darrieus-Landau model (a), and eddy map (b).

4.3 Darrieus-Landau model sensitivity

The sensitivity of the results to the Darrieus-Landau (DL) model is shown in Fig. 10 (a), which compares Cases 2 and 11 in Table 1 at $y = 1.69$ m. Without the DL model, the temperature profile is reduced near the wall and at the furthest measurement positions. The DL model acts on density differences in an accelerating flow. As the wall is stationary, the effects of dilatation are cumulative in accelerating the flow away from the wall. Conversely, as the flow is accelerated upwards due to buoyancy, fluid is drawn in from the surroundings which tends to counteract the positive dilatation of heat release. Fig. 10 (b) shows the eddy maps for the DL and no DL cases. Without the DL model there are fewer eddies, and the eddies occur locations nearer the wall. The ODT parameters can be adjusted to compensate for the depressed temperature away from the wall, but in doing so, the mixing rates are increased and the temperatures near the wall are then too low.

4.4 Thermocouple analysis

In the previous results, the modeled gas temperature is compared to the experimental thermocouple reading. A model thermocouple temperature for Case 2 is implemented and tested here. This is done assuming equilibrium between a model thermocouple and the surrounding gas temperature, that is, the net heat transfer to the thermocouple is zero,

$$\epsilon \left(\frac{1}{2}q^+ + \frac{1}{2}q^- - \sigma T_t^4 \right) + h_c(T_g - T_t) = 0, \tag{10}$$

where ϵ is the thermocouple emissivity, h_c is the heat transfer coefficient, σ is the Stefan-Boltzmann constant, and T_g, and T_t are the gas and thermocouple temperatures, respectively. Here, a model thermocouple temperature corresponding to the model gas temperature is evaluated at every point in the domain for each
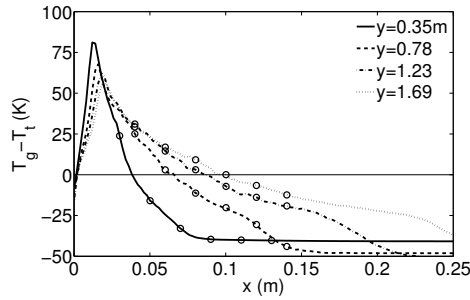
Fig. 11 Temperature difference profile between the gas and thermocouple model for Case 2 at four heights. Symbols correspond to the location of the experimental measurements.

realization, and the results are averaged. The heat transfer coefficient h_c is computed from $Nu = hD/k$ and $Nu = 2 + 0.6Re^{1/2}Pr^{1/3}$, where local composition, temperature, and pressure dependent properties are used. The thermocouple bead diameter is taken as 2.5 times the wire diameter, and the emissivity is taken as 0.6, as oxidized alumel and chromel. The difference between the mean gas and thermocouple temperatures are shown in Fig. 11. The difference is fairly small in the measurement region. The maximum magnitude difference of the mean temperatures in Fig. 11 in the measurement region is 40 K and 29 K at $y = 0.35$ and $y = 1.69$ m, respectively. The average magnitude difference in the measurement region is 30 K and 11 K at $y = 0.35$ and $y = 1.69$ m, respectively. Lower emissivities result in smaller differences. Using $\epsilon = 0.2$ as suggested in [45] for type-K thermocouples, the maximum magnitude difference of the mean temperatures in the measurement region is 14 K and 11 K at $y = 0.35$ and $y = 1.69$ m, respectively. The differences were also smaller for the isothermal boundary condition Case 10.

The upper range of a type-K thermoucouple is around 1600 K, and the peak fluctuating temperature measurement was 1663 K. The effect of limiting the upper temperature was tested by processing the ODT with all temperatures above above 1600 K truncated to 1600 K. Figure 12 compares mean and RMS temperature profiles with and without temperature truncation. There is little variation in the mean temperature, though the RMS profile decreases by up to 70 K when the temperature is truncated. The differences are less at lower heights, and at lower flow rates.

The thermocouples have a reported response time of 50 ms in air at 5 m/s (which is close to the simulated peak mean velocity). The following expression may be used to relate the RMS thermocouple temperature to the RMS gas temperature [46]:

$$\frac{T_{rms,g}}{T_{rms,t}} = \sqrt{1 + \omega^2\tau^2}, \tag{11}$$

where ω is the fluctuating gas frequency and τ is the thermocouple response time. Here, $dT_t/dt = (T_g - T_t)/\tau$ is used. Finney et al. [5] reported power spectra with frequencies up to 20 Hz. At 5, 10, and 20 Hz, the RMS gas temprature would be 3%, 12%, and 41% higher than the RMS thermocouple temperature, respectively. Any limitations in data sampling frequency would further reduce measured RMS temperatures.

(a)   (b)
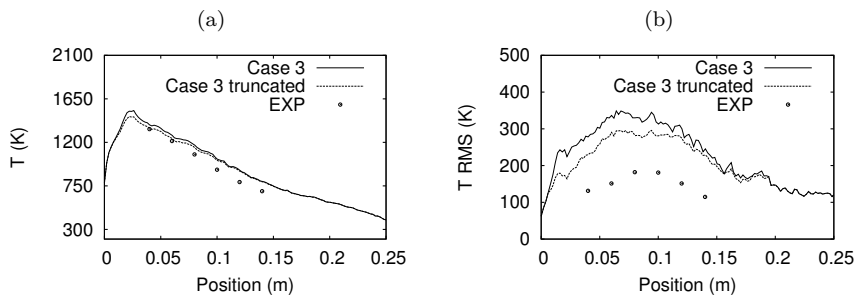
Fig. 12 Comparison of mean (a) and RMS (b) temperature profiles at $y = 1.69$ m when temperature data is truncated downwards to 1600 K.

5 Conclusions

ODT simulations have been performed of an ethylene wall flame using a consistent spatial formulation. The model was compared with experimental results in which ethylene is fed at varying flow rates through a porous wall burner. The configuration was chosen to mimic the behavior of a turbulent flame brush at the interface of a nominally vertical flame front in a wildland fire propagating through a dense fuel bed. Other wall fire applications are relevant. As combustion gases rise, flames become inclined due to flame dilatation and they are dispersed laterally by turbulence. In such flows, flame spread by direct flame contact has been found to be important.

The ODT model resolves diffusion-reaction flame structures in one dimension, with physically realistic turbulent statistics arising through the advective processes in the model. This allows details of temperature fluctuations to be modeled. ODT simulation results were presented of mean and fluctuating temperature, soot, and velocity profiles. Agreement with experimental results is generally good.

A new Darrieus-Landau (DL) instability model was implemented within ODT that accounts for instabilities arising from dilatation-induced acceleration in a variable density flow. The model had a significant effect on the results. This model can be applied to any ODT of combustion processes.

A number of simulations were performed in which flow rate, ODT parameters, boundary conditions, chemistry model, and the DL instability were varied or tested. ODT showed correct trends with increasing flow rate, and results were found to be most sensitive to the β parameter, followed by the C parameter, with little sensitivity to Z. Small-to-modest variations in mean temperatures were found when varying the boundary condition, and chemistry model. Thermocouple temperatures were estimated to differ from gas temperatures by less than 40 K in the measurement region.

The detailed flame structure information, and multiscale resolution capabilities of ODT, combined with the relative cost-effectiveness are advantages of the model. Further applications towards model validation and development, such as quantifying subgrid uncertainties in chemistry, soot, and radiation models are areas of future interest.

References

1. D. Drysdale, *An Introduction to Fire Dynamics*, 3rd edn. (Wiley Interscience, 2011)
2. W. Pitts, Progress in Energy and Combustion Science **17**, 83 (1991)
3. R.O. Weber, Progress in Energy and Combustion **17**, 67 (1991)
4. P.G. Baines, Mathematical and Computer Modelling **13**, 83 (1990)
5. M. Finney, D. Jimenez, J. Cohen, I. Grenfell, C. Wold, in *VI International Conference on Forest Fire Research* (2010)
6. J. Cohen, M. Finney, in *VI International Conference on Forest Fire Research* (2010)
7. K. Yedinak, J.D. Cohen, J. Forthofer, M. Finney, International Journal of Wildland Fire **19**, 171 (2010)
8. A.R. Kerstein, Journal of Fluid Mechanics **392**, 277 (1999)
9. A.R. Kerstein, W.T. Ashurst, S. Wunsch, V. Nilsen, Journal of Fluid Mechanics **447**, 85 (2001)
10. R.C. Schmidt, A.R. Kerstein, S. Wunsch, V. Nilsen, Journal of Computational Physics **186**, 317 (2003)
11. S. Wunsch, A.R. Kerstein, Journal of Fluid Mechanics **528**, 173 (2005)
12. E. Gonzalez-Juez, A.R. Kerstein, D.O. Lignell, Journal of Fluid Mechanics **677**, 218 (2011)
13. T.D. Dreeben, A.R. Kerstein, International Journal of Heat and Mass Transfer **43**, 3823 (2000)
14. D.O. Lignell, D. Rappleye, Combustion and Flame **159**, 2930 (2012)
15. N. Punati, J.C. Sutherland, A.R. Kerstein, E.R. Hawkes, J.H. Chen, Proceedings of the Combustion Institute **33**, 1515 (2011)
16. J.C. Hewson, A.R. Kerstein, Combustion Theory and Modelling **5**, 669 (2001)
17. J.C. Hewson, A.R. Kerstein, Combustion Science and Technology **174**, 35 (2002)
18. T. Echekki, A.R. Kerstein, T.D. Dreeben, Combustion and Flame **125**, 1083 (2001)
19. A.J. Ricks, J.C. Hewson, A.R. Kerstein, J.P. Gore, S.R. Tieszen, W.T. Ashurst, Combustion Science and Technology **182**, 60 (2010)
20. H. Shihn, P.E. DesJardin, International Journal of Heat and Mass Transfer **50**, 1314 (2007)
21. H. Shihn, P.E. DesJardin, in *Proceedings of IMECE04 ASME International Mechanical Engineering Congress and Exposition, Anaheim, CA* (November 13-20, 2004)
22. A.R. Kerstein, Computer Physics Communications **148**, 1 (2002)
23. R.C. Schmidt, A.R. Kerstein, R. McDermott, Comput. Methods Appl. Mech. Engrg. **199**, 865 (2010)
24. R.J. McDermott, Toward one-dimensional turbulence subgrid closure for large-eddy simulation. Ph.D. thesis, The University of Utah (2005)
25. S. Cao, T. Echekki, Journal of Turbulence **9**, 1 (2008)
26. T. Ahmad, G.M. Faeth, Proceedings of the Combustion Institute **17**, 1149 (1979)
27. G.H. Markstein, J.D. Ris, Proc. Combust. Inst. **24**, 1747 (1992)
28. J. Quintiere, Fire Safety Journal **3**, 201 (1981)
29. M.A. Delichatsios, Proceedings of the Combustion Institute **21**, 53 (1986)
30. P. Joulain, Fire Safety Journal **26**, 99 (1996)
31. H. Wang, M. Coutin, J. Most, Fire Safety Journal **37**, 259 (2002)
32. W.T. Ashurst, A.R. Kerstein, Physics of Fluids **17-025107**, 1 (2005)
33. D.O. Lignell, A.R. Kerstein, G. Sun, E.I. Monson, Theoretical and Computational Fluid Dynamics **27**, 273 (2013)
34. P.A. Lewis, G.S. Shedler, Naval Res. Logistics Quart. **26**, 403 (1979)
35. A. Papoulis, S.U. Pillai, *Probability, Random Variables, and Stochastic Processes*, 4th edn. (McGraw-Hill, New York, 2002)
36. D. Goodwin. Cantera, an object-oriented software toolkit for chemical kinetics, thermodynamics, and transport processes (2011). http://code.google.com/p/cantera
37. S. Cohen, A. Hindmarsh, Compututational Physics **10**, 138 (1996). http://llnl.gov/casc/sundials/
38. E. Gonzalez-Juez, A.R. Kerstein, D.O. Lignell, Geophysical and Astrophysical Fluid Dynamics **107**, 506 (2013)
39. C.K. Westbrook, F.L. Dryer, Combustion Science and Technology **27**, 31 (1981)

40. D.O. Lignell, J.H. Chen, P.J. Smith, T. Lu, C.K. Law, Combustion and Flame **151**, 2 (2007)
41. K.M. Leung, R.P. Lindstedt, Combustion and Flame **87**, 289 (1991)
42. N. Peters, Progress in Energy and Combustion Science **10**, 319 (1984)
43. M.F. Modest, *Radiative Heat Transfer* (McGraw-Hill, New York, 1993)
44. Y. Ju, H. Guo, K. Maruta, F. Liu, Journal of Fluid Mechanics **342**, 315 (1997)
45. C.R. Shaddix, in *NHTC99-282, 33rd National Heat Transfer Conference*. Albuquerque, NM, (1999)
46. G. Csanady, Journal of Atmospheric Science **20**, 201 (1963)